

Strong Spin-Lattice Interaction in Layered Antiferromagnetic CrCl_3

Łucja Kipczak^{1,*}, Tomasz Woźniak,^{1,2} Chinmay K. Mohanty,¹ Igor Antoniazzi,¹ Jakub Iwański¹, Przemysław Oliwa¹, Jan Pawłowski,¹ Meganathan Kalaiarasan,³ Zdeněk Sofer,³ Andrzej Wysmołek¹, Adam Babiński¹, Maciej Koperski^{1,4,5} and Maciej R. Molas^{1,†}

¹Faculty of Physics, University of Warsaw, Pasteura 5, 02-093 Warsaw, Poland

²Faculty of Fundamental Problems of Technology, Wrocław University of Science and Technology, Wyb. Wyspiańskiego 27, 50-370 Wrocław, Poland

³Department of Inorganic Chemistry, University of Chemistry and Technology, Technická 5, 160 00 Praha 6-Dejvice, Prague, Czech Republic

⁴Institute for Functional Intelligent Materials, National University of Singapore, 9 Engineering Dr 1, 117544, Singapore

⁵Department of Materials Science and Engineering, National University of Singapore, 9 Engineering Dr 1, 117575, Singapore

Understanding the coupling between lattice vibrations and magnetic order is crucial for controlling properties of two-dimensional magnetic materials. Here, we investigate the vibrational properties of bulk and thick-flake CrCl_3 using polarization-resolved Raman spectroscopy, complemented by photoluminescence, photoluminescence excitation, and optical absorption measurements. Symmetry analysis, supported by first-principles phonon calculations, enables the unambiguous assignment of all eight Raman-active modes, four A_g and four E_g , previously predicted only theoretically. Excitation-energy-dependent measurements reveal that the strong enhancement of selected phonon modes originates primarily from interference effects rather than resonant Raman scattering. Temperature-dependent Raman spectroscopy further reveals pronounced signatures of spin-phonon coupling across the transition from a fully antiferromagnetic phase, through an intermediate regime with local, domain-like ferromagnetic order, to the paramagnetic phase, accompanied by a clear rhombohedral-to-monoclinic structural transition. Together, these results demonstrate how lattice, electronic, and magnetic degrees of freedom collectively govern the Raman response of CrCl_3 .

The discovery of a long-range magnetism in two-dimensional (2D) van der Waals (vdW) materials has opened new opportunities to explore magnetic phenomena in reduced dimensionality and to integrate magnetic order into layered heterostructures. Furthermore, interplay between sample thickness, external magnetic fields, and optical excitations governs the stabilization of the magnetic ordering, including the formation of topological spin textures.^{1–3} These advances substantially broaden the scope of spintronic,^{4,5} valleytronic,⁶ and quantum magneto-optical applications.^{7–11}

Chromium trihalides, with the chemical formula CrX_3 ($\text{X} = \text{Cl}, \text{Br}, \text{I}$), constitute a prototypical family of vdW magnetic materials. In bulk CrX_3 , strong intralayer ferromagnetic (FM) coupling is present within each $\text{X}-\text{Cr}-\text{X}$ layer; however, both the magnetic anisotropy and the interlayer exchange interactions vary markedly across the halide series. In particular, CrCl_3 exhibits antiferromagnetic (AFM) interlayer coupling and an in-plane easy axis,^{12–15} in sharp contrast to the heavier chromium trihalides. On the other hand, CrBr_3 displays FM interlayer coupling and strong out-of-plane magnetic anisotropy, resulting in spins aligned perpendicular to the layers,^{16,17} whereas CrI_3 , despite its pronounced out-of-plane anisotropy arising from strong spin-orbit coupling, exhibits AFM interlayer coupling in the bilayer and few-layer limits.^{13,18,19} Moreover, the interlayer magnetic coupling is highly sensitive to the stacking order. Stacking faults commonly occur in these materials due to the small energy differences between competing crystallographic structures, and such structural variations can

strongly impact the magnetic order.²⁰

Beyond their intrinsic magnetic and structural properties, CrX_3 compounds are well suited for vdW heterostructures, in which magnetic layers are combined with nonmagnetic semiconductors or other 2D materials. In such hybrid systems, interfacial proximity effects enable the transfer of magnetic order, exchange fields, or spin textures to adjacent layers.^{21–25} These engineered heterostructures provide a versatile platform for the realization of novel spin-based and magneto-optical devices.

In this work, we investigate spin-phonon interactions in bulk CrCl_3 and thick exfoliated flakes using Raman scattering (RS) and complementary optical spectroscopies. Polarization-resolved RS measurements, combined with first-principles phonon calculations, enable the symmetry assignment of all eight Raman-active phonon modes, four A_g and four E_g modes, completing their experimental verification beyond theoretical predictions. Excitation-energy-dependent RS and optical spectroscopy show that interference effects dominate the enhancement of the Raman response. Temperature-dependent Raman measurements uncover strong spin-phonon coupling and reveal pronounced anomalies at the magnetic ordering temperature, together with a clear rhombohedral-to-monoclinic structural transition.

CrCl_3 crystallizes in a monoclinic structure with $C2/m$ symmetry at ambient temperature and undergoes a transition to a rhombohedral phase upon cooling.¹³ At low temperature ($T \sim 10$ K), CrCl_3 adopts $R\bar{3}$ symmetry, corresponding to a primitive rhombohedral unit cell belonging to space group No. 148.^{12,26–28} Figures 1(a)–(c) illus-

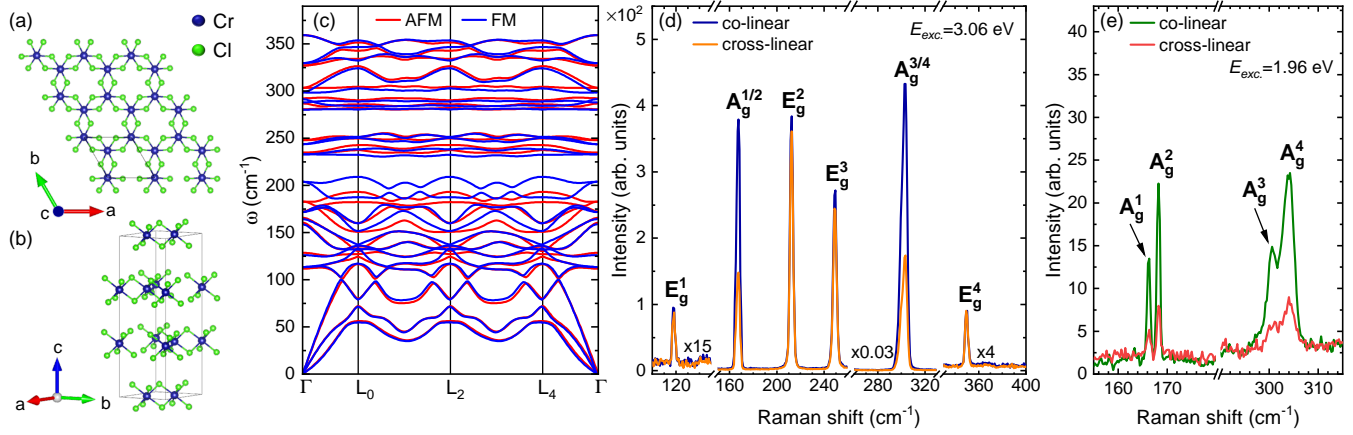


FIG. 1. Schematic representation of the rhombohedral crystal structure of CrCl₃. (a) Top view of a monolayer, with the unit cell indicated by a black rectangle and shown in a simplified form for clarity. (b) Perspective view of the bulk structure, illustrating the stacking of CrCl₃ layers along the *c*-axis and the arrangement of multiple layers within the unit cell. (c) Phonon dispersion of bulk CrCl₃ calculated for the rhombohedral primitive cell with ferromagnetic (blue) and antiferromagnetic (red) spin configurations. (d) and (e) Low-temperature ($T=5$ K) Raman scattering spectra of bulk CrCl₃ measured in co-linear and cross-linear polarization configurations using 3.06 eV and 1.96 eV laser excitation, respectively, with a laser power of 75 μ W. Panel (e) is limited to two A_g modes exhibiting doublet structures.

trate the crystal structure of the rhombohedral CrCl₃, including a top view of a monolayer (a) and the bulk stacking sequence (b). Within each layer, Cr atoms form a hexagonal lattice, with each Cr atom octahedrally coordinated by six chlorine (Cl) atoms through strong covalent bonding. Adjacent layers are coupled by weak vdW interactions,^{9,12} which enable mechanical exfoliation.^{13,29,30} Phonon dispersions, shown in Fig. 1(c), were calculated for both the AFM and FM phases using density functional theory (DFT) in light of recent reports of coexisting magnetic orders in bulk CrCl₃.³¹ The computational details are provided in the Methods section of the Supporting Information (SI). The calculated lattice constant $a=6.7069$ Å and rhombohedral angle $\alpha=52.9688^\circ$ agree well with the experimentally reported values of $a=6.7194$ Å and $\alpha=52.4825^\circ$ measured at $T=225$ K.³² At the Γ point, eight Raman-active phonon modes are obtained for both AFM and FM orders, which can be classified according to the irreducible representation $\Gamma_{\text{AFM/FM}}=4\text{A}_\text{g}+4\text{E}_\text{g}$.

We investigated the phonon modes of bulk CrCl₃, *i.e.*, a macroscopic single crystal, as described in the Methods section of the SI. Polarization-resolved low-temperature ($T=5$ K) RS spectra of bulk CrCl₃, measured using 3.06 eV excitation, are presented in Fig. 1(d). Six Raman-active modes are experimentally resolved, consisting of two modes with A_g symmetry and four modes with E_g symmetry. The numerical superscripts assigned to the modes serve solely as labels and do not denote their symmetry character.

The mode assignments were established through polarization-resolved RS measurements performed in co-linear and cross-linear configurations. As shown in the

figure, the intensities of the E_g modes remain essentially unchanged between the two polarization geometries, whereas the A_g modes are strongly suppressed, by approximately a factor of three, in the cross-linear configuration. Because the A_g symmetry peaks exhibit asymmetric line shapes under 3.06 eV excitation, additional polarization-resolved RS measurements were carried out using 1.96 eV excitation to achieve improved spectral resolution (Fig. 1(e)). These measurements clearly demonstrate that both the A_g^{1/2} and A_g^{3/4} features consist of two well-resolved peaks, each exhibiting A_g symmetry. To rule out sample-quality effects related to crystal growth, complementary measurements were performed on a commercially available CrCl₃ crystal, which displays an identical double-peak structure for these modes (see Section S1 of the SI). Experimental artifacts can also be excluded, as the double-peak structure is observed exclusively for the A_g^{1/2} and A_g^{3/4} modes, whereas all other Raman-active modes consistently exhibit single, well-defined peaks.

These results establish that the low-temperature RS spectra of bulk CrCl₃ comprise eight phonon modes, *i.e.*, four A_g and four E_g modes, in full agreement with theoretical predictions for both AFM and FM orders. Table I compares the calculated phonon frequencies with the experimentally measured Raman modes and shows excellent overall agreement. While the polarization behavior of the E_g modes follows symmetry-based selection rules, the A_g modes are expected to vanish entirely in the cross-linear configuration.^{33–35} The finite A_g intensities observed under cross-linear polarization are attributed to resonant excitation effects, as previously reported for thin layers of semiconducting transition metal

dichalcogenides.^{36,37} Angle-resolved RS measurements, presented in Section S2 of the SI, further confirm the isotropic in-plane symmetry of bulk CrCl₃.

To evaluate the influence of excitation energy on the RS spectra, we measured low-temperature RS spectra of bulk CrCl₃ using multiple excitation energies, *i.e.*, 3.06 eV, 2.54 eV, 2.41 eV, 2.21 eV, and 1.96 eV, as shown in Fig. 2(a). The Raman modes intensities are comparable for most excitation energies, whereas a pronounced enhancement is observed under the 3.06 eV excitation. For clarity, the spectrum acquired at 3.06 eV is scaled by a factor of 0.04, and the spectral region between 100 cm⁻¹ and 130 cm⁻¹ is further magnified by a factor of 15 to highlight all Raman features. Across all excitation energies, six Raman-active modes are observed, consistent with previous reports on CrCl₃ crystals.^{28,38,39} To clarify the role of the excitation energy, the behavior of individual Raman modes is analyzed below.

The E_g¹ mode is detected exclusively under 3.06 eV excitation and remains substantially weaker than the other modes. The E_g² mode, together with the A_g^{1/2} and A_g^{3/4} doublets, exhibits a non-monotonic dependence on excitation energy (discussed in detail below) and reaches maximum relative intensity at 2.21 eV. In contrast, the E_g³ and E_g⁴ modes display nearly identical excitation-energy dependences: their intensities are strongly suppressed as the excitation energy decreases from 3.06 to 2.41 eV, become barely discernible at 2.21 eV, and vanish entirely at 1.96 eV.

To probe the origin of the resonant Raman response in CrCl₃, we extracted the integrated intensities of the E_g², A_g^{1/2}, and A_g^{3/4} modes by Lorentzian deconvolution of the spectra for all excitation energies, as shown in Fig. 2(b). The intensities of the A_g^{1/2} and A_g^{3/4} modes are treated as a combined doublet intensity, since their individual contributions cannot be reliably deconvoluted under 3.06 eV excitation. The extracted phonon intensities span nearly two orders of magnitude, underscoring the presence of

strong enhancement effects.

The intensity of the RS signal in vdW materials is known to depend sensitively on the excitation energy.^{40–43} Within a simple picture, resonant enhancement of RS, governed by electron-phonon coupling, occurs when the excitation energy approaches an electronic or excitonic transition of the material.⁴⁰ To identify transitions relevant to the resonant conditions of RS in CrCl₃, we measured the photoluminescence excitation (PLE) spectrum by monitoring the broad photoluminescence (PL) band of bulk CrCl₃ while continuously tuning the excitation energy, as shown in Fig. 2(b). The PL spectrum of bulk CrCl₃ is characteristic of a molecular crystal, with Frenkel-type excitons localized on individual molecules and radiative recombination governed by the Franck-Condon principle.^{44–46} The PLE spectrum reveals two broad excitation bands centered at approximately 1.89 eV and 2.38 eV. The lower-energy band consists of two resonances at about 1.79 eV and 1.94 eV, while the higher-energy band comprises three resonances at approximately 2.20 eV, 2.34 eV, and 2.56 eV. We further measured the absorbance (Abs) spectrum of a CrCl₃ crystal, shown in Fig. 2(b). The Abs spectrum exhibits two peaks centered at approximately 1.76 eV and 2.38 eV, which are attributed to the so-called A and B excitons,^{13,44,45,47} followed by a pronounced absorption onset at higher photon energies near 3.15 eV. A detailed analysis of these absorption features is presented below.

Comparison of the excitation-energy-dependent phonon intensities with the PLE and Abs spectra partially accounts for the observed variations in Raman intensity. For all excitation energies except 3.06 eV, the evolution of the Raman peak intensities qualitatively follows the shape of the PLE spectrum, suggesting the coupling between the excited states responsible for PL emission and phonons via exciton–phonon interactions. In contrast, the pronounced enhancement of the Raman signal under 3.06 eV excitation does not coincide with any prominent feature in either the PLE or Abs spectra, indicating that it is not of electronic-resonant origin.

Instead, this enhancement points to optical interference effects as the dominant mechanism. To test this hypothesis, we simulated the excitation-energy dependence of the E_g², A_g^{1/2}, and A_g^{3/4} intensities using the transfer matrix method (TMM)⁴⁸ and the complex refractive index of a CrCl₃ crystal with a thickness of approximately 92 μ m (see the Methods section of the SI for details). The calculations were performed using the complex refractive index determined at room temperature ($T=300$ K).⁴⁵ As shown in Fig. 2(c), the simulated A_g^{3/4} intensity exhibits a strong enhancement for excitation energies above approximately 2.85 eV, while reaching a minimum near 2.35 eV. Simulations for the E_g² and A_g^{1/2} modes are presented in Section S3 of the SI. A detailed comparison between the calculated excitation-energy dependence of the A_g^{3/4} intensity at 300 K and the experimentally extracted inte-

TABLE I. Comparison of vibrational mode frequencies observed experimentally and calculated using DFT.

Mode	Experiment	DFT calculations	
		FM phase	AFM phase
E _g ¹	118.7 cm ⁻¹	113.5 cm ⁻¹	111.9 cm ⁻¹
A _g ¹	166.1 cm ⁻¹	158.7 cm ⁻¹	160.5 cm ⁻¹
A _g ²	168.2 cm ⁻¹	164.2 cm ⁻¹	165.7 cm ⁻¹
E _g ²	212.8 cm ⁻¹	203.8 cm ⁻¹	182.8 cm ⁻¹
E _g ³	249.5 cm ⁻¹	233.0 cm ⁻¹	234.6 cm ⁻¹
A _g ³	300.5 cm ⁻¹	280.3 cm ⁻¹	280.8 cm ⁻¹
A _g ⁴	303.9 cm ⁻¹	281.2 cm ⁻¹	286.9 cm ⁻¹
E _g ⁴	350.3 cm ⁻¹	329.7 cm ⁻¹	327.0 cm ⁻¹

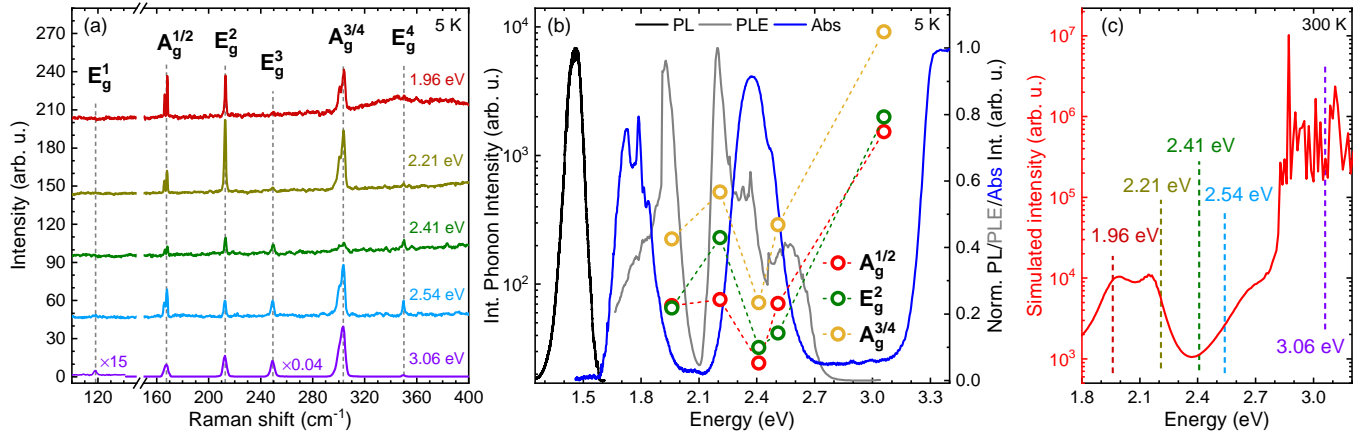


FIG. 2. Resonant Raman scattering investigation in the CrCl₃ crystal. (a) Raman scattering spectra of the CrCl₃ crystal measured at 5 K using different excitation energies: 1.96 eV, 2.21 eV, 2.41 eV, 2.54 eV, 3.06 eV, with an excitation power of 50 μ W. The spectra have been vertically shifted for better visual clarity. (b) Left axis: graph shows points representing the intensity of individual Raman modes present in every spectra collected with different excitation lasers (in logarithmic scale). Right axis: normalized PL (black), PLE (grey) and Abs (blue) spectra measured on the CrCl₃ crystal. The PL spectrum was measured with 2.21 eV laser with power around 0.5 μ W. The PLE spectrum was detected via supercontinuum laser with power around 2 μ W. (c) Simulated enhancement of the Ag^{3/4} intensity using the transfer-matrix method. The colored vertical dashed lines indicate the excitation energies used in the experiment.

grated intensity at 5 K shows excellent overall agreement. In particular, the large enhancement of the Raman signal under 3.06 eV excitation is fully reproduced by the simulated interference effects, despite the difference between the experimental and simulation temperatures. Taken together, the combined effects of resonant Raman scattering and optical interference within the CrCl₃/SiO₂/Si dielectric stack provide a comprehensive description of the excitation-energy dependence of the RS intensity.

A similar analysis of excitation-energy effects for an exfoliated CrCl₃ flake with a thickness of approximately 227 nm, together with corresponding TMM simulations, is presented in Section S4 of the SI.

The combined PL and Abs measurements enable the determination of the electronic band gap (E_g) of CrCl₃ as well as the exciton binding energies (E_b), as shown in Fig. 2(b). The exciton binding energy is evaluated using the relation $E_b = E_g - E_{ex}$, where E_{ex} denotes the excitonic peak energy. The band gap E_g is extracted using the Tauc method⁴⁹, expressed as $(\alpha h\nu)^\gamma = A(h\nu - E_g)$, where α is the absorption coefficient, A is a proportionality constant, and γ characterizes the nature of the electronic transition ($\gamma = 2$ for a direct band gap). From this analysis, the electronic band gap of CrCl₃ is estimated to be ~ 3.2 eV. The found E_b energies of the A and B excitons from the absorption measurements are approximately 1.45 eV and 0.82 eV, respectively, in good agreement with previously reported values.⁴⁵ The PL emission peak at 1.47 eV originates from the same excitonic state as the absorption feature at 1.76 eV (A exciton) and is redshifted due to the $d-p$ hybridization between Cr and ligand states.^{44,50} Accordingly, the binding energy asso-

ciated with the A-exciton emission is estimated to be ~ 1.73 eV.

To elucidate the lattice dynamics and the coupling between phonons and magnetic order in bulk CrCl₃, we performed temperature-dependent RS measurements under 3.06 eV excitation from 5 K to 300 K. The overall evolution of the phonon modes is summarized in the false-color intensity map shown in the top panel of Fig. 3(a), with a representative RS spectrum acquired at 5 K displayed in the bottom panel. The intensities in both panels are plotted on a logarithmic scale to enhance the visibility of weaker features. A closer inspection of the false-color map reveals distinct temperature-dependent behaviors for different phonon modes. The intensities of the E_g¹ and E_g⁴ modes decrease markedly with increasing temperature and vanish completely from the spectra at approximately 140 K and 190 K, respectively. In contrast, the remaining modes, *i.e.*, A_g^{1/2}, E_g², E_g³, and A_g^{3/4}, remain clearly observable across the entire temperature range. Notably, the background intensity increases at elevated temperatures and reaches a maximum near 220 K, which may be associated with a broad temperature range of coexistence between the rhombohedral and monoclinic phases, extending approximately from 140 K to 240 K.^{13,51}

Deconvolution of the temperature-dependent RS spectra using Lorentzian functions enables a detailed analysis of the temperature evolution of the Raman shifts, linewidths (full width at half-maximum, FWHM), and intensities of all six resolved phonon modes. The corresponding Raman shifts are shown in Fig. 3(b)-(g) and discussed below, while the linewidths and intensities are analyzed in Section S5 of the SI.

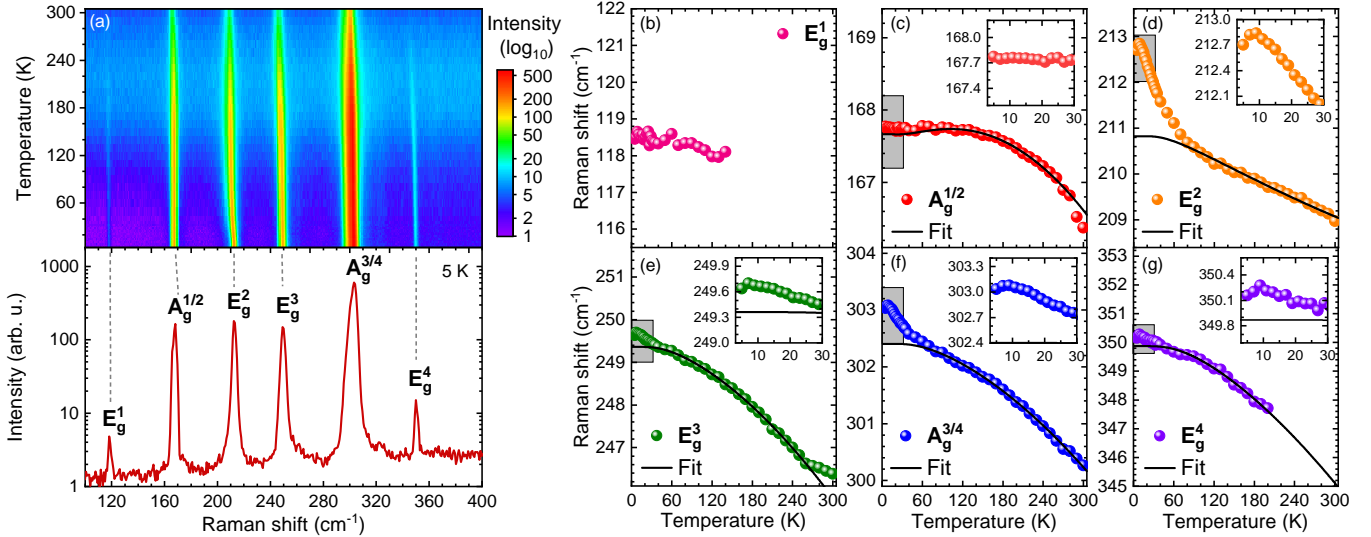


FIG. 3. Temperature evolution of the Raman modes. (a) The top panel shows a false-color map of the Raman spectra of a CrCl₃ crystal, while the bottom panel presents the Raman spectrum measured at $T=5$ K. The intensities are plotted on a logarithmic scale to better visualize the temperature dependence of the Raman shifts for all observed modes. (b)–(g) Temperature dependence of the Raman shift for all observed phonon modes. Solid lines represent fits using Eq. 1. The insets show the low-temperature range of the frequency evolution of the modes, as indicated by the gray rectangular regions.

To assess the spin-lattice coupling, the temperature dependence of the phonon energies was fitted using the standard Balkanski model, which describes anharmonic phonon softening with increasing temperature due to phonon-phonon interactions.⁵² The model is given by

$$\omega_{anh}(T) = \omega_0 + A \left(1 + \frac{2}{e^x + 1} \right) + B \left(1 + \frac{3}{e^y - 1} + \frac{3}{(e^y - 1)^2} \right), \quad (1)$$

where ω_0 , A , and B are fitting parameters, $x = \frac{\hbar\omega_0}{2k_B T}$, and $y = \frac{\hbar\omega_0}{3k_B T}$. The quantity $\omega_0 + A + B$ corresponds to the phonon frequency extrapolated to 0 K.

The temperature evolution of the A_g^{1/2} mode is well described by the Balkanski model, indicating that this phonon is only weakly affected by magnetic interactions and behaves predominantly as a classical anharmonic mode governed by phonon-phonon scattering.^{53,54} In contrast, the remaining modes (E_g², E_g³, A_g^{3/4}, and E_g⁴) exhibit clear deviations from the standard anharmonic behavior,^{52,55–57} particularly in the low-temperature regime between 5 K and 80 K.

A detailed inspection of this temperature range reveals that, for all these modes, the Raman shift increases slightly as the temperature rises from 5 K to approximately 10 K. This temperature range is close to the Néel temperature ($T_N=14$ K) of CrCl₃, which marks the transition from the AFM phase to the paramagnetic order.^{58,59} The magnitude of the anomalous redshift between 5 K and 80 K varies substantially among the modes. The E_g² mode exhibits the strongest anomaly,

with an energy shift of approximately 2.0 cm⁻¹, whereas the E_g³ and E_g⁴ modes show intermediate shifts of about 0.6 cm⁻¹. The A_g^{3/4} mode displays a comparable shift of approximately 0.7 cm⁻¹. At higher temperatures (80 K–300 K), the slopes of the experimental data change, and the phonon energies recover a conventional anharmonic temperature dependence similar to that observed in both magnetic and nonmagnetic materials.^{55–57}

The presence of anomalous temperature-dependent behavior, not accounted for by anharmonic effects, in the majority of phonon modes up to approximately 80 K strongly suggests that magnetic ordering in CrCl₃ persists to temperatures well above the Néel temperature. The most plausible scenario therefore involves three distinct magnetic regimes in CrCl₃. At $T < T_N$, CrCl₃ exhibits fully developed AFM order, characterized by FM ordering within individual layers and AFM coupling between adjacent layers. Notably, ferromagnetic ordering persisting above T_N has already been reported for thick exfoliated CrCl₃ flakes.²⁴ In the intermediate temperature range $T_N < T < 80$ K, a locally ordered magnetic state emerges, in which FM correlations persist within individual layers in a domain-like structure, while interlayer AFM order is suppressed. Because the phonon modes examined here involve exclusively intralayer atomic vibrations within a single CrCl₃ layer, the observed anomalies indicate that local FM order within individual layers survives up to temperatures of approximately 80 K. At higher temperatures ($T > 80$ K), CrCl₃ enters a purely paramagnetic phase.

The temperature evolution of the Raman modes pro-

TABLE II. Spin-phonon coupling constant (λ) values of Raman modes

	E_g^2	E_g^3	$A_g^{3/4}$	E_g^4
λ	0.94 cm ⁻¹	0.28 cm ⁻¹	0.35 cm ⁻¹	0.28 cm ⁻¹

vides a clear signature of the structural phase transition in bulk CrCl_3 from the low-temperature rhombohedral ($\bar{R}3$) phase to the high-temperature monoclinic ($C2/m$) phase, with phase coexistence between approximately 140 K and 240 K.^{13,51} As shown in Fig. 3(a), the RS spectra undergo a pronounced transformation upon warming. The coexistence regime is particularly evident in the E_g^3 mode (Fig. 3(e)), which exhibits a change in slope near 250 K, indicating completion of the transition to the monoclinic phase. Low-intensity modes such as E_g^1 and E_g^4 become unobservable at elevated temperatures due to weak Raman cross sections and thermal broadening, although they are expected to persist, consistent with previous reports⁶⁰ and phonon calculations for the monoclinic phase.³⁹ In addition, the E_g^2 , E_g^3 , and $A_g^{3/4}$ modes exhibit strong intensity suppression above ~ 160 K, marking the onset of structural instability in the rhombohedral lattice (see Section S5 of the SI). Overall, the Raman data confirm that the rhombohedral ($\bar{R}3$) phase is stable up to ~ 140 K, followed by a broad transition to monoclinic ($C2/m$) symmetry that is fully established above 240 K.^{13,51}

The corresponding analysis of the temperature dependence of the RS spectra of the exfoliated CrCl_3 flake, presented in Section S6 of the SI, demonstrates behavior similar to that discussed above for the bulk CrCl_3 crystal.

The strength of the spin-phonon interaction at 5 K was quantified by extracting the spin-phonon coupling coefficients (λ) using the commonly employed relation:^{61–64}

$$\omega(T) \simeq \omega_{\text{anh}}(T) + \lambda \langle s_i \cdot s_j \rangle, \quad (2)$$

where $\omega(T)$ is the measured phonon frequency, $\omega_{\text{anh}}(T)$ is the anharmonic phonon frequency in the absence of spin-phonon coupling, λ is the spin-phonon coupling constant, and $\langle s_i \cdot s_j \rangle$ denotes the nearest-neighbor spin-spin correlation function.^{61–65} For Cr^{3+} ions with spin $S = 3/2$, $\langle s_i \cdot s_j \rangle = 9/4$, consistent with the magnetic moment of approximately $3\mu_B$.^{13,58,66–69} The extracted values of the spin-phonon coupling constants are summarized in Table II. The strongest coupling is observed for the E_g^2 mode, with $\lambda \approx 0.94$ cm⁻¹. The $A_g^{3/4}$, E_g^3 , and E_g^4 modes exhibit smaller yet still significant coupling strengths of approximately 0.35 cm⁻¹, 0.28 cm⁻¹, and 0.28 cm⁻¹, respectively.

To contextualize these findings, we compare our results with those reported in the literature for the other magnetic materials. The coupling strengths determined for the modes $A_g^{3/4}$, E_g^3 and E_g^4 are comparable to the values observed in CrBr_3 , where λ for the E_g mode is

reported as 0.27 cm⁻¹,⁶² 0.43 cm⁻¹,⁶³ and up to 0.51 cm⁻¹,⁶¹ as well as in CrSBr ($\lambda = 0.29$ cm⁻¹ for the A_g mode).⁶⁴ Remarkably, the strong coupling identified for the E_g^2 mode approaches the substantial values found in heavy-element tellurides, such as $\text{Cr}_2\text{Ge}_2\text{Te}_6$, where λ reaches 0.82 cm⁻¹⁷⁰ and 1.2 cm⁻¹ for the E_g mode⁷¹ and Fe_2GeTe_2 - $\lambda = 1.3$ cm⁻¹ for the A_g mode.⁷²

In summary, we have systematically investigated the vibrational properties of bulk and thick-flake CrCl_3 using polarization-resolved RS spectroscopy in combination with PL, PLE, and Abs measurements. Using symmetry analysis and first-principles phonon calculations, we achieve an unambiguous experimental assignment of all eight Raman-active phonon modes, comprising four A_g and four E_g modes. Excitation-energy-dependent measurements demonstrate that the pronounced enhancement of selected phonon modes is governed primarily by optical interference effects rather than by resonant Raman scattering. Temperature-dependent Raman spectroscopy reveals strong signatures of spin-phonon coupling, indicating the persistence of local magnetic correlations well above the antiferromagnetic ordering temperature and delineating a transition from a fully antiferromagnetic phase through an intermediate domain-like ferromagnetic regime to a paramagnetic state. In addition, clear Raman signatures of a rhombohedral-to-monoclinic structural phase transition are observed. These results highlight the intricate interplay between lattice, electronic, and magnetic degrees of freedom in CrCl_3 and establish Raman spectroscopy as a powerful probe of spin-lattice coupling in layered magnetic materials.

DATA AVAILABILITY

The data that support the findings of this work are available from the corresponding authors upon reasonable request.

ACKNOWLEDGMENTS

The work was supported by the National Science Centre, Poland (grant no. 2020/37/B/ST3/02311, 2023/48/C/ST3/00309). T.W. gratefully acknowledges Poland's high-performance Infrastructure PLGrid ACC Cyfronet AGH for providing computer facilities and support within computational Grant No. PLG/2025/018073. Z.S. was supported by project LUAUS25268 from Ministry of Education Youth and Sports (MEYS) and by the project Advanced Functional Nanorobots (reg. no. CZ.02.1.01/0.0/0.0/15_003/0000444 financed by the EFRR). Z.S. acknowledges the assistance provided by the Advanced Multiscale Materials for Key Enabling Technologies project, supported by the Ministry of Educa-

tion, Youth, and Sports of the Czech Republic (project no. CZ.02.01.01/00/22_008/0004558), co-funded by the European Union. M.K. acknowledges the Ministry of Education (Singapore) through the Research Centre of Excellence program (grant EDUN C-33-18-279-V12, I-FIM) and under its Academic Research Fund Tier 2 (MOE-T2EP50122-0012), and the Air Force Office of Scientific Research and the Office of Naval Research Global under award number FA8655-21-1-7026.

AUTHOR CONTRIBUTIONS

M.R.M. initiated and supervised the project. L.K. prepared the CrCl_3 samples and performed the RS and PL measurements. Ł.K. and J.P. performed the AFM imaging. T.W. calculated the phonon dispersion using density functional theory (DFT). Ł.K. and I.A. carried out the PLE experiment. C.K.M., J.I., and A.W. carried out the absorption measurements. P.O. and Ł.K. simulated the interference effects. M.K. (Prague) and Z.S. grew the CrCl_3 crystals. Ł.K. analyzed the experimental data with contributions from A.B., M.K. (Singapore), and M.R.M. Ł.K and M.R.M. wrote the manuscript with input from all co-authors.

* lucja.kipczak@fuw.edu.pl

† maciej.molas@fuw.edu.pl

- [1] S. Grebenchuk, C. McKeever, M. Grzeszczyk, Z. Chen, M. Šiškins, A. R. C. McCray, Y. Li, A. K. Petford-Long, C. M. Phatak, D. Ruihuan, L. Zheng, K. S. Novoselov, E. J. G. Santos, and M. Koperski, *Advanced Materials* **36**, 2311949 (2024).
- [2] S. Grebenchuk, M. Grzeszczyk, Z. Chen, K. S. Novoselov, and M. Koperski, *Journal of Physics: Materials* **7**, 035009 (2024).
- [3] J. Fullerton, Y. Li, H. Solanki, S. Grebenchuk, M. Grzeszczyk, Z. Chen, M. Šiškins, K. S. Novoselov, M. Koperski, E. J. G. Santos, and C. Phatak, *Advanced Materials* **n/a**, e13067 (2025).
- [4] M. Mi, H. Xiao, L. Yu, Y. Zhang, Y. Wang, Q. Cao, and Y. Wang, *Materials Today Nano* **24**, 100408 (2023).
- [5] Z. Jia, M. Zhao, Q. Chen, Y. Tian, L. Liu, F. Zhang, D. Zhang, Y. Ji, B. Camargo, K. Ye, R. Sun, Z. Wang, and Y. Jiang, *ACS Nano* **19**, 9452 (2025).
- [6] C. Luo, Z. Huang, H. Qiao, X. Qi, and X. Peng, *Journal of Physics: Materials* **7**, 022006 (2024).
- [7] S. Jiang, L. Li, Z. Wang, K. F. Mak, and J. Shan, *Nature Nanotechnology* **13**, 549 (2018).
- [8] B. Huang, G. Clark, D. R. Klein, D. MacNeill, E. Navarro-Moratalla, K. L. Seyler, N. Wilson, M. A. McGuire, D. H. Cobden, D. Xiao, W. Yao, P. Jarillo-Herrero, and X. Xu, *Nature Nanotechnology* **13**, 544 (2018).
- [9] M. Gilbertini, M. Koperski, A. F. Morpurgo, and K. S. Novoselov, *Nature Nanotechnology* **14**, 408 (2019).
- [10] D. Soriano, M. I. Katsnelson, and J. Fernández-Rossier, *Nano Letters* **20**, 6225 (2020).
- [11] Q. H. Wang, A. Bedoya-Pinto, M. Blei, A. H. Dismukes, A. Hamo, S. Jenkins, M. Koperski, Y. Liu, Q.-C. Sun, E. J. Telford, H. H. Kim, M. Augustin, U. Vool, J.-X. Yin, L. H. Li, A. Falin, C. R. Dean, F. Casanova, R. F. L. Evans, M. Chshiev, A. Mishchenko, C. Petrovic, R. He, L. Zhao, A. W. Tsen, B. D. Gerardot, M. Brotons-Gisbert, Z. Guguchia, X. Roy, S. Tongay, Z. Wang, M. Z. Hasan, J. Wrachtrup, A. Yacoby, A. Fert, S. Parkin, K. S. Novoselov, P. Dai, L. Balicas, and E. J. G. Santos, *ACS Nano* **16**, 6960 (2022).
- [12] M. A. McGuire, *Crystals* **7**, 121 (2017).
- [13] M. A. McGuire, G. Clark, S. KC, W. M. Chance, G. E. Jellison, V. R. Cooper, X. Xu, and B. C. Sales, *Phys. Rev. Mater.* **1**, 014001 (2017).
- [14] K. F. Mak, J. Shan, and D. C. Ralph, *Nature Reviews Physics* **1**, 646 (2019).
- [15] M. Serri, G. Cucinotta, L. Poggini, G. Serrano, P. Sainctavit, J. Strychalska-Nowak, A. Politano, F. Bonacorso, A. Caneschi, R. J. Cava, R. Sessoli, L. Ottaviano, T. Klimczuk, V. Pellegrini, and M. Mannini, *Advanced Materials* **32**, 2000566 (2020).
- [16] J. F. Dillon Jr, H. Kamimura, and R. J. P., *Journal of Applied Physics* **34**, 1240 (1963).
- [17] J. Dillon, H. Kamimura, and J. Remeika, *Journal of Physics and Chemistry of Solids* **27**, 1531 (1966).
- [18] M. A. McGuire, H. Dixit, V. R. Cooper, and B. C. Sales, *Chemistry of Materials* **27**, 612 (2015).
- [19] S. Li, Z. Ye, X. Luo, G. Ye, H. H. Kim, B. Yang, S. Tian, C. Li, H. Lei, A. W. Tsen, K. Sun, R. He, and L. Zhao, *Phys. Rev. X* **10**, 011075 (2020).
- [20] S. Y. Grebenchuk, M. Grzeszczyk, Z. Chen, M. Šiškins, V. Borisov, M. Pereiro, M. I. Katsnelson, O. Eriksson, K. S. Novoselov, and M. Koperski, *Advanced Science* **12**, 2500562 (2025).
- [21] M.-C. Heißenbüttel, T. Deilmann, P. Krüger, and M. Rohlfing, *Nano Letters* **21**, 5173 (2021).
- [22] S. K. Behera, M. Bora, S. S. Paul Chowdhury, and P. Deb, *Phys. Chem. Chem. Phys.* **21**, 25788 (2019).
- [23] L. Ciorciaro, M. Kroner, K. Watanabe, T. Taniguchi, and A. Imamoglu, *Phys. Rev. Lett.* **124**, 197401 (2020).
- [24] L. Kipczak, Z. Chen, M. Grzeszczyk, S. Grebenchuk, P. Huang, K. Vaklinova, K. Watanabe, T. Taniguchi, A. Babiński, M. Koperski, and M. R. Molas, *Nanoscale Horiz.* **10**, 2465 (2025).
- [25] D. Jana, S. Mukherjee, D. Litvinov, M. Grzeszczyk, S. Grebenchuk, M. Šiškins, V. Gavriliuc, Y. Ouyang, C. Chen, Y. Ye, M. Yiming, and M. Koperski, *Advanced Functional Materials* **n/a**, e16728 (2025).
- [26] J. Cable, M. Wilkinson, and E. Wollan, *Journal of Physics and Chemistry of Solids* **19**, 29 (1961).
- [27] K. B., *Physica Status Solidi (A)* **72**, 161 (1982).
- [28] I. Kanesaka, H. Kawahara, A. Yamazaki, and K. Kawai, *Journal of Molecular Structure* **146**, 41 (1986).
- [29] J. Liu, Q. Sun, Y. Kawazoe, and P. Jena, *Phys. Chem. Chem. Phys.* **18**, 8777 (2016).
- [30] L. Webster and J.-A. Yan, *Phys. Rev. B* **98**, 144411 (2018).
- [31] J. A. Schneeloch, A. A. Aczel, F. Ye, and D. Louca, *Phys. Rev. B* **110**, 144439 (2024).
- [32] B. Morosin and A. Narath, *The Journal of Chemical Physics* **40**, 1958 (1964).

[33] D. R. Klein, D. MacNeill, Q. Song, D. T. Larson, S. Fang, M. Xu, R. A. Ribeiro, P. C. Canfield, E. Kaxiras, R. Comin, and P. Jarillo-Herrero, *Nature Physics* **15**, 1255 (2019).

[34] B. Huang, J. Cenker, X. Zhang, E. L. Ray, T. Song, T. Taniguchi, K. Watanabe, M. A. McGuire, D. Xiao, and X. Xu, *Nature Nanotechnology* **15**, 212 (2020).

[35] T. T. Mai, K. F. Garrity, A. McCreary, J. Argo, J. R. Simpson, V. Doan-Nguyen, R. V. Aguilar, and A. R. H. Walker, *Science Advances* **7**, eabj3106 (2021).

[36] J.-U. Lee and H. Cheong, *Journal of Raman Spectroscopy* **49**, 66 (2018).

[37] Q.-H. Tan, Y.-J. Sun, X.-L. Liu, K.-X. Xu, Y.-F. Gao, S.-L. Ren, P.-H. Tan, and J. Zhang, *Nano Research* **14**, 239 (2021).

[38] V. M. Bermudez, *Solid State Communications* **19**, 693 (1976).

[39] S. Kazim, M. Ali, S. Palleschi, G. D'Olimpio, D. Mazzatorta, A. Politano, R. Gunnella, A. D. Cicco, M. Renzelli, G. Moccia, O. A. Cacioppo, R. Alfonsi, J. Strychalska-Nowak, T. Klimczuk, R. J. Cava, and L. Ottaviano, *Nanotechnology* **31**, 395706 (2020).

[40] B. R. Carvalho, L. M. Malard, J. M. Alves, C. Fantini, and M. A. Pimenta, *Phys. Rev. Lett.* **114**, 136403 (2015).

[41] X. Zhang, X.-F. Qiao, W. Shi, J.-B. Wu, D.-S. Jiang, and P.-H. Tan, *Chemical Society Reviews* **44**, 2757 (2015).

[42] M. Grzeszczyk, K. Gołasa, M. Zinkiewicz, K. Nogański, M. R. Molas, M. Potemski, A. Wysmołek, and A. Babiński, *2D Materials* **3**, 025010 (2016).

[43] H. P. C. Miranda, S. Reichardt, G. Froehlicher, A. Molina-Sánchez, S. Berciaud, and L. Wirtz, *Nano Letters* **17**, 2381 (2017).

[44] S. Acharya, D. Pashov, A. N. Rudenko, M. Rösner, M. v. Schilfgaarde, and M. I. Katsnelson, *npj 2D Materials and Applications* **6**, 33 (2022).

[45] G. Ermolaev, T. Mazitov, A. Minnekhanov, A. Mazitov, G. Tselikov, A. Slavich, A. P. Tsapenko, M. Tatmyshhevskiy, M. Kashchenko, N. Pak, A. Vyshnevyy, A. Melentev, E. Zhukova, D. Grudinin, J. Luo, I. Kruglov, A. Arsenin, S. Zhao, K. S. Novoselov, A. Katanin, and V. S. Volkov, *Magnetic excitons in non-magnetic crcl3* (2025), arXiv:2505.00920 [cond-mat.mtrl-sci].

[46] M. Grzeszczyk, S. Acharya, D. Pashov, Z. Chen, K. Vaklinova, M. van Schilfgaarde, K. Watanabe, T. Taniguchi, K. S. Novoselov, M. I. Katsnelson, and M. Koperski, *Advanced Materials* **35**, 2209513 (2023).

[47] L. Zhu and L. Yang, *Phys. Rev. B* **101**, 245401 (2020).

[48] N. V. Velson, H. Zobeiri, and X. Wang, *Opt. Express* **28**, 35272 (2020).

[49] P. Makuła, M. Pacia, and W. Macyk, *The Journal of Physical Chemistry Letters* **9**, 6814 (2018).

[50] K. L. Seyler, D. Zhong, D. R. Klein, S. Gao, X. Zhang, B. Huang, E. Navarro-Moratalla, L. Yang, D. H. Cobden, M. A. McGuire, W. Yao, D. Xiao, P. Jarillo-Herrero, and X. Xu, *Nature Physics* **14**, 277 (2018).

[51] O. N. Lis, D. P. Kozlenko, E. V. Lukin, S. E. Kichanov, I. Y. Zel, A. V. Belushkin, S. S. Agafonov, P. A. Borisova, and B. N. Savenko, *Phys. Rev. B* **112**, 104105 (2025).

[52] M. Balkanski, R. F. Wallis, and E. Haro, *Phys. Rev. B* **28**, 1928 (1983).

[53] X. Yan, B. Wang, Y. Hai, D. R. Kripalani, Q. Ke, and Y. Cai, *Science China Physics, Mechanics & Astronomy* **65**, 117004 (2022).

[54] K. Wilczyński, A. P. Gertych, and M. Zdrojek, *Acta Materialia* **294**, 121133 (2025).

[55] A. Taube, A. Łapińska, J. Judek, and M. Zdrojek, *Applied Physics Letters* **107**, 013105 (2015).

[56] J. Joshi, I. R. Stone, R. Beams, S. Krylyuk, I. Kalish, A. V. Davydov, and P. M. Vora, *Applied Physics Letters* **109**, 031903 (2016).

[57] S. Sarkar, I. Maity, H. L. Pradeepa, G. Nayak, L. Marty, J. Renard, J. Coraux, N. Bendjab, V. Bouchiat, S. Das, K. Majumdar, M. Jain, and A. Bid, *Phys. Rev. B* **101**, 205302 (2020).

[58] C. A. Pocs, I. A. Leahy, H. Zheng, G. Cao, E.-S. Choi, S.-H. Do, K.-Y. Choi, B. Normand, and M. Lee, *Phys. Rev. Res.* **2**, 013059 (2020).

[59] N. Bykovetz, A. Hoser, and C. L. Lin, *AIP Advances* **9**, 035029 (2019).

[60] A. Glazamza, P. Lemmens, S.-H. Do, Y. S. Kwon, and K.-Y. Choi, *Phys. Rev. B* **95**, 174429 (2017).

[61] T. Yin, K. A. Ulman, S. Liu, A. Granados del Águila, Y. Huang, L. Zhang, M. Serra, D. Sedmidubsky, Z. Sofer, S. Y. Quek, and Q. Xiong, *Advanced Materials* **33**, 2101618 (2021).

[62] D. P. Kozlenko, O. N. Lis, S. E. Kichanov, E. V. Lukin, N. M. Belozerova, and B. N. Savenko, *npj Quantum Materials* **6**, 19 (2021).

[63] Ł. Kipczak, A. Karmakar, M. Grzeszczyk, R. Janiszewska, T. Woźniak, Z. Chen, J. Pawłowski, K. Watanabe, T. Taniguchi, A. Babiński, M. Koperski, and M. R. Molas, *Scientific Reports* **14**, 7484 (2024).

[64] X. Wei, M. Li, X. He, Q. Xie, L. Chen, L. Ma, and G. Cheng, *Applied Physics Letters* **126**, 252201 (2025).

[65] K.-z. Lili Hu, Y. Du, Y. Chen, X. Zhai, and Q. X. Wang, *National Science Open* **2**, 20230002 (2023).

[66] M. Grodzicki, B. Mallick, and A.-V. Mudring, *Journal of Physics: Conference Series* **200**, 032020 (2010).

[67] X. Lu, R. Fei, L. Zhu, and L. Yang, *Nature Communications* **11**, 4724 (2020).

[68] A. Bedoya-Pinto, J.-R. Ji, A. K. Pandeya, P. Gargiani, M. Valvidares, P. Sessi, J. M. Taylor, F. Radu, K. Chang, and S. S. P. Parkin, *Science* **374**, 616 (2021).

[69] G. Buccoliero, P. Vasconcelos Borges Pinho, M. dos Reis Cantarino, F. Rosa, N. B. Brookes, and R. Sant, *Advanced Materials Interfaces* **12**, e00229 (2025).

[70] G. Krasucki, K. Olkowska-Pucko, T. Woźniak, M. I. Sturza, H. Kohlmann, A. Babiński, and M. R. Molas, *Spin-phonon coupling and isotope-related pseudo-molecule vibrations in layered cr₂ge₂te₆ ferromagnet* (2025), arXiv:2510.01881 [cond-mat.mtrl-sci].

[71] Y. Tian, M. J. Gray, H. Ji, R. J. Cava, and K. S. Burch, *2D Materials* **3**, 025035 (2016).

[72] L. Du, J. Tang, Y. Zhao, X. Li, R. Yang, X. Hu, X. Bai, X. Wang, K. Watanabe, T. Taniguchi, D. Shi, G. Yu, X. Bai, T. Hasan, G. Zhang, and Z. Sun, *Advanced Functional Materials* **29**, 1904734 (2019).

[73] A. Castellanos-Gómez, M. Buscema, R. Molenaar, V. Singh, L. Janssen, H. S. J. van der Zant, and G. A. Steele, *2D Materials* **1**, 011002 (2014).

[74] I. H. Malitson, *J. Opt. Soc. Am.* **55**, 1205 (1965).

[75] D. Franta, A. Dubroka, C. Wang, A. Giglia, J. Vohánka, P. Franta, and I. Ohlídal, *Applied Surface Science* **421**, 405 (2017).

[76] G. Kresse and J. Hafner, *Phys. Rev. B* **47**, 558 (1993).

[77] G. Kresse and J. Hafner, *Phys. Rev. B* **49**, 14251 (1994).

- [78] G. Kresse and J. Furthmüller, *Computational Materials Science* **6**, 15 (1996).
- [79] G. Kresse and J. Furthmüller, *Phys. Rev. B* **54**, 11169 (1996).
- [80] G. Kresse and D. Joubert, *Phys. Rev. B* **59**, 1758 (1999).
- [81] S. Grimme, J. Antony, S. Ehrlich, and H. Krieg, *The Journal of Chemical Physics* **132**, 154104 (2010).
- [82] X. Li, S.-H. Do, J. Yan, M. A. McGuire, G. E. Granroth, S. Mu, T. Berlijn, V. R. Cooper, A. D. Christianson, and L. Lindsay, *Acta Materialia* **241**, 118390 (2022).
- [83] A. Togo, L. Chaput, T. Tadano, and I. Tanaka, *Journal of Physics: Condensed Matter* **35**, 353001 (2023).
- [84] A. Togo, *Journal of the Physical Society of Japan* **92**, 012001 (2023).
- [85] J. Menéndez and M. Cardona, *Phys. Rev. B* **29**, 2051 (1984).

Supporting Information: Strong Spin-Lattice Interaction in Layered Antiferromagnetic CrCl₃

Lucja Kipczak¹, Tomasz Woźniak,^{1,2} Chinmay K. Mohanty,¹ Igor Antoniazzi,¹ Jakub Iwański¹, Przemysław Oliwa¹,¹ Jan Pawłowski,¹ Meganathan Kalaiarasan,³ Zdeněk Sofer,³ Andrzej Wysmołek¹, Adam Babiński¹, Maciej Koperski^{1,4,5} and Maciej R. Molas¹

¹ Faculty of Physics, University of Warsaw, Pasteura 5, 02-093 Warsaw, Poland

² Faculty of Fundamental Problems of Technology, Wrocław University of Science and Technology, Wyb. Wyspiańskiego 27, 50-370 Wrocław, Poland

³ Department of Inorganic Chemistry, University of Chemistry and Technology, Technická 5, 160 00 Praha 6-Dejvice, Prague, Czech Republic

⁴ Institute for Functional Intelligent Materials, National University of Singapore, 9 Engineering Dr 1, 117544, Singapore

⁵ Department of Materials Science and Engineering, National University of Singapore, 9 Engineering Dr 1, 117575, Singapore

This Supporting Information provides: - Details of the crystal synthesis, samples fabrication, experimental setups, transfer matrix method simulations, and first principles calculations. **S1** - Raman scattering spectra of a commercial CrCl₃ crystal. **S2** - Angle-resolved polarization of phonon modes in CrCl₃ crystal. **S3** - Transfer matrix method simulations of phonon mode intensities in CrCl₃. **S4** - Angle-resolved and excitation-dependent Raman spectra of an exfoliated CrCl₃ flake. **S5** - Temperature evolution of the Raman mode intensities and linewidths in the CrCl₃ crystal. **S6** - Temperature-dependent Raman spectra of an exfoliated CrCl₃ flake.

Crystal synthesis

CrCl₃ crystals were prepared from polycrystalline material using the chemical vapor transport method in quartz ampoule. 30 g of CrCl₃ (99.9%, Strem, USA) were placed in quartz ampoule (50×250 mm) and degassed under high vacuum (<1×10⁻³ Pa, oil diffusion pump with LN₂ cold trap) at 100°C for 2 hours and subsequently melt sealed using oxygen-hydrogen welding torch. The ampoule was placed in a two zone horizontal furnace for crystal growth. The growth zone was first heated at 1000°C and the source zone at 700°C for 2 days. Subsequently, the thermal gradient was reversed and the source zone was heated at 900°C and the growth zone at 800°C for 15 days. Finally, the ampoule was cooled to room temperature and opened in an argon filled glovebox.

Samples fabrication

For Raman scattering (RS), photoluminescence (PL), and photoluminescence excitation (PLE) measurements, a bulk CrCl₃ crystal was mechanically placed on a silicon substrate coated with a 90 nm-thick SiO₂ layer. An optical micrograph of the sample is shown in Fig. **S1(a)**.

The crystal thickness at the Raman measurement position, indicated by the green rectangle in Fig. **S1(a)**, was determined by stylus profilometry. The height profile was acquired using a Veeco Dektak 6M profilometer equipped with a stylus 10 μm × 2 μm ASP, over a scan area of 16 mm² as shown in Fig. **S1(b)**. The thickness at this location was approximately 92.0 μm. The maximum height observed across the full scan range reached approximately 140 μm, which lies outside the region displayed in the optical image.

For absorption measurements, the CrCl₃ crystal was mounted on a copper plate containing a 1 mm-diameter aperture.

Thick exfoliated CrCl₃ flakes were prepared from bulk crystals using a polydimethylsiloxane (PDMS)-based exfoliation method and subsequently transferred onto SiO₂/Si substrates with a 285 nm-thick SiO₂ layer via an all-dry deterministic stamping technique, which avoids glue residues.⁷³ The thickness of the investigated CrCl₃ flake was determined by atomic force microscopy (AFM) using a Bruker Dimension Icon system equipped with a NanoScope VI controller. AFM measurements were performed in PeakForce Tapping mode under ambient conditions using a silicon probe (RFESP-75 model). The flake thickness was found to be approximately 227 nm, as shown in Fig. **S2**.

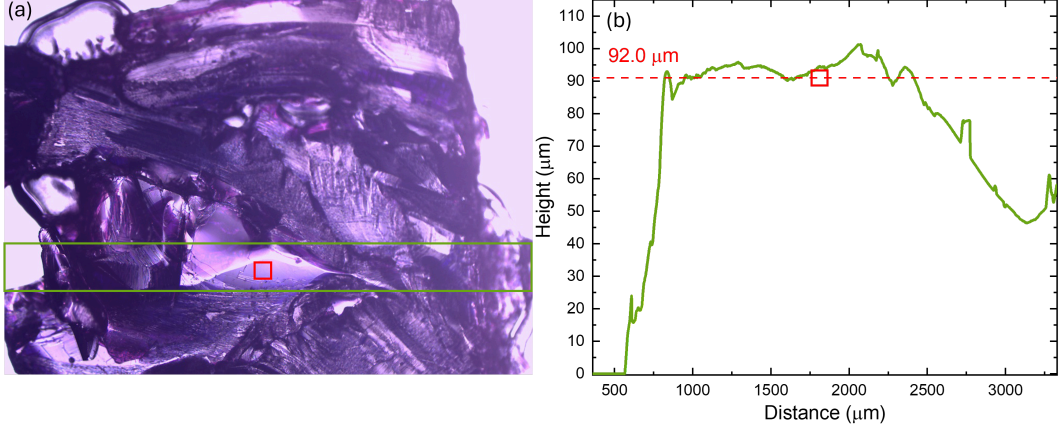


FIG. S1. (a) Optical image of the investigated CrCl_3 crystal. The green rectangle indicates the scanning area profiled by the stylus (center of rectangle), while the red square marks the spot selected for Raman measurements. (b) Topographical profile corresponding to the region marked in (a). The green curve shows the height variation across the sample. The dashed red line indicates the thickness at the Raman measurement spot (marked by the red square), which is 92.0 μm . Note that the distance axis has been offset to align the scan range with the optical image's field of view.

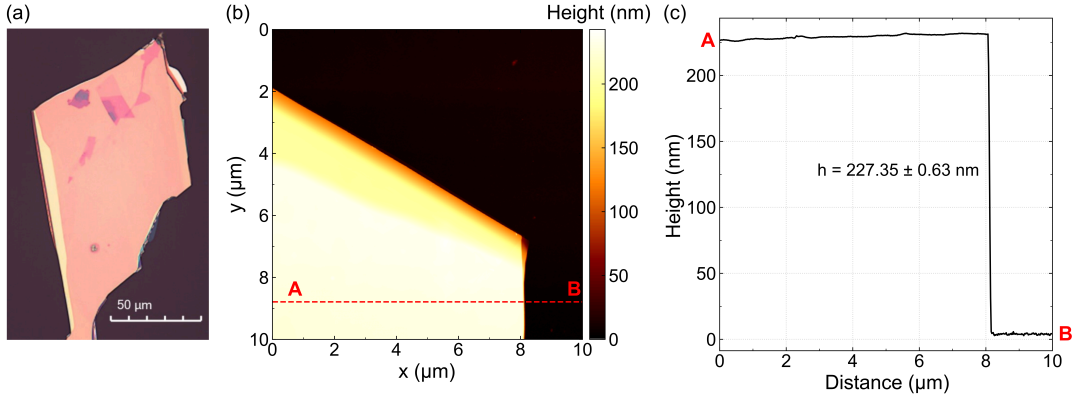


FIG. S2. (a) Optical image of the investigated CrCl_3 flake. The red square indicates the probed area. (b) Atomic force microscopy (AFM) topography of the investigated flake. The red line (A-B) marks the location of the cross-section used for thickness determination. (c) Height profile extracted along the line (A-B) revealing a flake thickness of $227.35 \pm 0.63 \text{ nm}$.

Raman scattering

RS spectra were excited using diode lasers with wavelengths of $\lambda = 405 \text{ nm}$ (3.06 eV), $\lambda = 515 \text{ nm}$ (2.41 eV), and $\lambda = 561 \text{ nm}$ (2.21 eV), as well as a He-Ne laser ($\lambda = 633 \text{ nm}$, 1.96 eV) and an Ar-ion laser ($\lambda = 488 \text{ nm}$, 2.54 eV). Samples were mounted on the cold finger of a continuous-flow cryostat, enabling measurements over a temperature range from $\sim 5 \text{ K}$ to room temperature (300 K). The excitation beam was focused using a $50\times$ long-working-distance objective with a numerical aperture (NA) of 0.55, yielding a spot size of $\sim 1 \mu\text{m}$ in diameter. The scattered light was collected by the same objective in a backscattering geometry, dispersed by a 0.75 m spectrometer equipped with an 1800 grooves/mm grating, and detected with a liquid-nitrogen-cooled charge-coupled device (CCD). Laser lines were suppressed prior to the spectrometer using long-pass filters (488 nm, 515 nm, 561 nm, and 633 nm) or Bragg-grating notch filters (405 nm). Polarization-resolved RS measurements were performed using a motorized half-wave plate and a fixed linear polarizer in the detection path.

Photoluminescence excitation.

PLE measurements were performed using a broadband supercontinuum light source spectrally filtered by a monochromator, producing a monochromatic excitation beam with a linewidth of approximately 2 nm. The excitation power at the sample was stabilized using an electrically controlled liquid crystal followed by a linear polarizer, operating in a feedback loop with a photodiode monitoring the optical power entering the probe. The PLE spectra were recorded using the same experimental setup as for the RS measurements, with the spectrometer grating replaced by a 300 grooves/mm grating.

Absorbance

Abs spectra of the CrCl_3 crystal were recorded over the 350–850 nm spectral range using a Cary 5000 UV–Vis–NIR spectrophotometer operated in double-beam mode. Low-temperature measurements were performed using an Oxford Instruments closed-cycle helium cryostat equipped with an ITC502 temperature controller. To eliminate contributions from the sample mount and the finite aperture size, Abs spectra were acquired for both the crystal and an empty aperture of identical dimensions. The reference spectrum was subsequently subtracted from the sample spectrum, yielding the absorbance signal originating exclusively from the crystal.

Transfer-matrix method

To investigate the impact of layer thickness and optical interference on the measurable intensity of Raman modes, a rigorous model based on the TMM was employed. This approach accounts for multiple reflections of both the incident laser field and the scattered Raman signal at all interfaces within the multilayer structure, as well as for Raman signal generation throughout the volume of the active material. The calculations were performed following the formalism described by Van Velson et al.⁴⁸.

The considered system consists of layers characterized by complex refractive indices $\tilde{n}_j = n_j + i\kappa_j$, where j denotes the layer index (air, CrCl_3 , SiO_2/Si substrate). Assuming normal incidence of light, the relationship between the electric field amplitudes E^+ (forward propagating wave) and E^- (backward propagating wave) at the layer boundaries is described by the interference matrix I_{jk} and the propagation matrix L_j :

$$I_{jk} = \frac{1}{t_{jk}} \begin{pmatrix} 1 & r_{jk} \\ r_{jk} & 1 \end{pmatrix}, L_j = \begin{pmatrix} e^{-i\beta_j d_j} & 0 \\ 0 & e^{i\beta_j d_j} \end{pmatrix}, \quad (3)$$

where r_{jk} and t_{jk} are the Fresnel reflection and transmission coefficients, d_j is the layer thickness, and $\beta_j = \frac{2\pi}{\lambda} \tilde{n}_j$ represents the propagation constant.

The calculation of the total Raman signal intensity (I_{Raman}) was divided into two stages. First, excitation field distribution. The local electric field amplitude of the incident laser, $E_{\text{exc.}}(x)$, was determined as a function of depth x within the active layer (CrCl_3). The local RS generation intensity at depth x is assumed to be proportional to the square of the electric field amplitude, $|E_{\text{exc.}}(x)|^2$. Second, Raman signal propagation. The Raman signal generated at depth x at the Raman wavelength λ_{Raman} was treated as a plane-wave source emitted in two directions: forward (into the substrate) and backward (toward the detector). The algorithm rigorously accounts for the discontinuity of the electric field at the generation point x . The total Raman signal intensity reaching the detector results from the interference of waves generated at all depths within the active layer. In the simulations, an incoherent summation of contributions from different depths was assumed, which is the standard approach for layers with thicknesses significantly exceeding the coherence length of the Raman process. The final intensity was calculated as an integral over the active layer thickness d_{active} using formula:

$$I_{\text{Raman}} \propto \int_0^{d_{\text{active}}} |E_{\text{exc.}}(x, \lambda_{\text{exc.}})|^2 \cdot [|E_{\text{out,back}}(x, \lambda_{\text{Raman}})|^2 + |E_{\text{out,forward}}(x, \lambda_{\text{Raman}})|^2] dx, \quad (4)$$

where E_{out} represents the efficiency of coupling the Raman signal from depth x to the outside of the system. Numerical integration was performed using adaptive quadrature methods implemented in Python. The simulations accounted for the dispersion of all constituent materials by interpolating the wavelength-dependent complex refractive index, $\tilde{n}(\lambda) = n(\lambda) + i\kappa(\lambda)$, where $n(\lambda)$ and $\kappa(\lambda)$ correspond to the refractive index and extinction coefficient, respectively, evaluated at both the excitation wavelength and the Raman-scattered wavelengths. The complex refractive indices were taken from the literature for CrCl_3 ⁴⁵, SiO_2 ⁷⁴, and Si ⁷⁵.

DFT calculations

The first-principles calculations were performed within the density functional theory (DFT) in the Vienna ab-initio simulation package (VASP)^{76–79}. The projector augment wave (PAW) potentials and general gradient approximation (GGA) of Pedew-Burke-Ernzerhof (PBE)⁸⁰ with D3 van der Waals correction⁸¹ were used. Spin-orbit coupling was not included due to its insignificant impact on geometrical parameters and phonon dispersion in this compound, as shown by Li *et al.* in Ref.⁸². The primitive cell vectors and atomic positions have been optimized until forces on atoms were lower than 10^{-5} eV/Å and stress tensor components were lower than 0.1 kbar. A plane wave basis set cutoff of 500 eV and a Γ -centered k-mesh $6\times 6\times 6$ were sufficient to converge the lattice constants with precision of 0.001 Å. An energy tolerance of 10^{-8} eV was used to converge the charge density in all calculations. The phonon dispersion was calculated in a $2\times 2\times 2$ supercell using the finite displacement method as implemented in Phonopy package^{83,84}. All the calculations were performed at temperature of 0 K.

S1. Raman scattering spectra of a commercial CrCl_3 crystal

To validate the influence of excitation energy on the Raman spectra across different samples, we performed a comparative study using a commercial CrCl_3 crystal purchased from HQ Graphene. Figure S3(a) shows low-temperature Raman spectra acquired using excitation energies of 3.06 eV, 2.54 eV, 2.41 eV, 2.21 eV, and 1.96 eV. Overall, the relative intensities of the Raman modes are comparable to those observed in the as-synthesized crystal discussed in the main text. Consistent with previous observations, the spectrum acquired with the 3.06 eV excitation was scaled by a factor of 0.03 for clarity. In addition, the spectral region between $100\text{--}130\text{ cm}^{-1}$ was multiplied by 1.5 to enhance the visibility of the weak E_g^1 mode. Furthermore, the spectrum measured using the 2.41 eV excitation was scaled by a factor of 5 to facilitate comparison. Despite this enhancement, the corresponding peaks remain only slightly above the background noise level. Nevertheless, the corresponding peaks remain only slightly above the background noise level.

The intensity dependence on excitation energy follows a trend analogous to that shown in Fig. 2(a) of the main text. Moreover, the doublet structure of the A_g modes near 168 cm^{-1} and 303 cm^{-1} is clearly resolved for the 1.96 eV excitation, as shown in Fig. S3(b).

Taken together, these results confirm the presence of all eight Raman-active modes predicted by the phonon dispersion calculations (Fig. 1(b) in the main text), which are consistently observed in CrCl_3 crystals obtained from two independent sources.

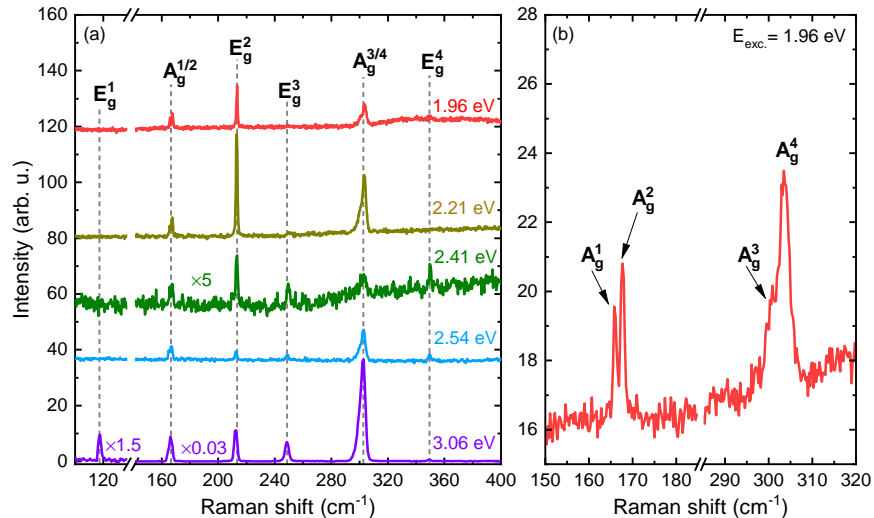


FIG. S3. Resonant Raman scattering measurements of a commercial CrCl_3 crystal. (a) Raman spectra of the CrCl_3 crystal acquired at $T = 5\text{ K}$ using excitation energies of 1.96 eV, 2.21 eV, 2.41 eV, 2.54 eV, and 3.06 eV with an excitation power of $75\text{ }\mu\text{W}$. The spectra are vertically shifted for clarity. (b) Low-temperature ($T = 5\text{ K}$) Raman spectrum of the same CrCl_3 crystal measured using 1.96 eV excitation, highlighting the doublet structure of two A_g modes.

S2. Angle-resolved polarization of phonon modes in CrCl_3 crystal

To determine the symmetry of the Raman-active modes in CrCl_3 , we measured their linear polarization dependence at low temperature ($T = 5$ K). The intensities of the Raman modes presented in Figs. S4(a), (c), (d), and (f) remain unchanged as a function of polarization angle. Therefore, the modes were assigned to the E_g symmetry and are associated with in-plane atomic vibrations within the crystal lattice. In contrast, the intensities of the modes shown in Figs. S4(b) and (e) exhibit a clear dependence on the polarization angle. For these modes, the experimental data was fitted using Eq. (5),

$$I(\theta) = I_0 + A \cos^2(\theta - \phi), \quad (5)$$

where I_0 denotes the background intensity, A is the amplitude of the intensity modulation, and ϕ is a phase offset. These modes are therefore assigned to the A_g symmetry and correspond to out-of-plane atomic vibrations.

In particular, the intensity of the A_g modes does not decrease to zero near a polarization angle of approximately 110° . This behavior is likely due to the resonant excitation effects, which was previously reported in the literature, for thin layers of TMDs.^{36,37} Because the polarization-dependent measurements were performed using a 3.06 eV excitation laser, for which the spectral resolution is lower than that obtained with the 1.96 eV excitation, the doublet structure of the A_g modes could not be resolved.

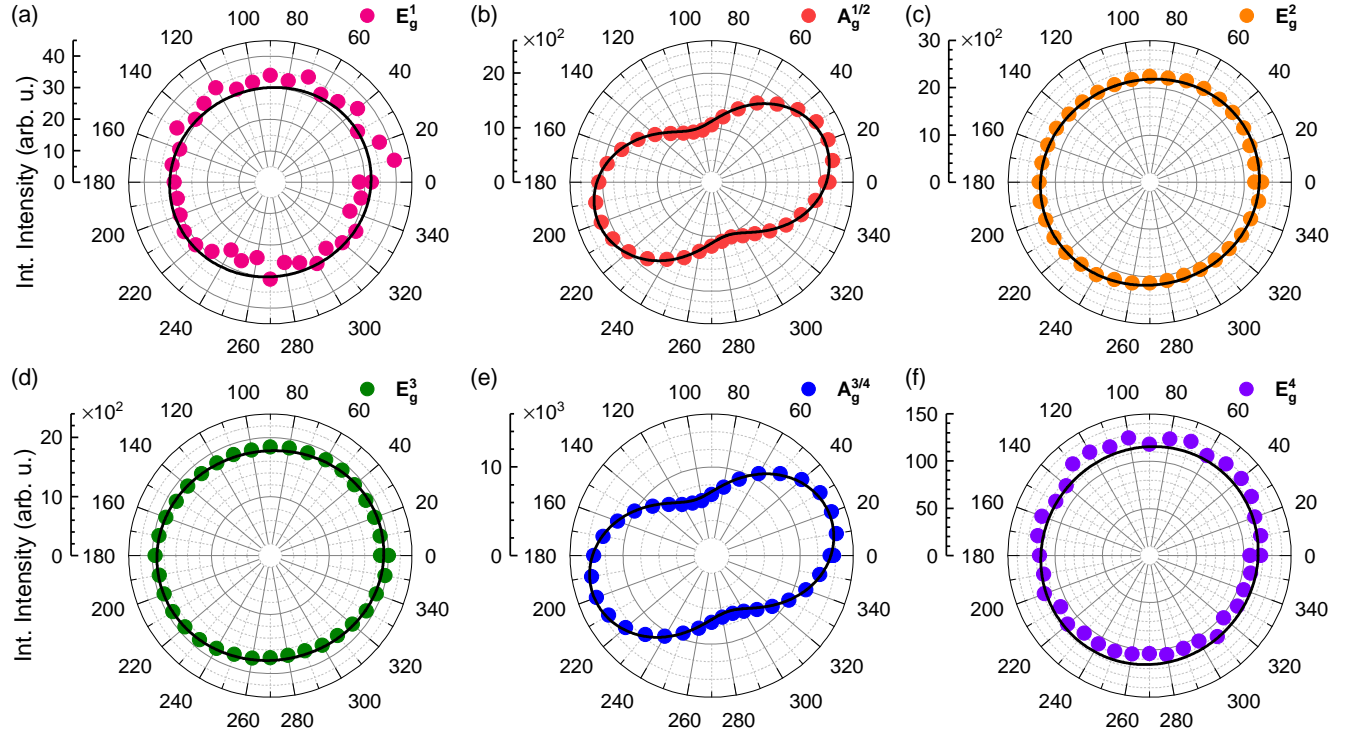


FIG. S4. Polarization dependence of the six Raman-active modes observed in the Raman spectra of a CrCl_3 crystal. Measurements were performed using a 3.06 eV laser at low temperature ($T=5$ K) with an excitation power of approximately $75 \mu\text{W}$. The modes shown in panels (a), (c), (d), and (f) correspond to the E_g symmetry, while those in panels (b) and (e) are of A_g symmetry. The black curves represent fits to Eq. (5).

S3. Transfer matrix method simulations of phonon mode intensities in CrCl_3

Figures S5(a) and (b) show the simulated Raman-mode intensities as a function of excitation energy for the $A_g^{1/2}$ and E_g^2 modes, respectively. The calculations were performed using the TMM method, described in the Methods section, at room temperature ($T=300$ K). The simulations follow the same procedure as that applied to the $A_g^{3/4}$ mode (see Fig. 2(c) in the main text).

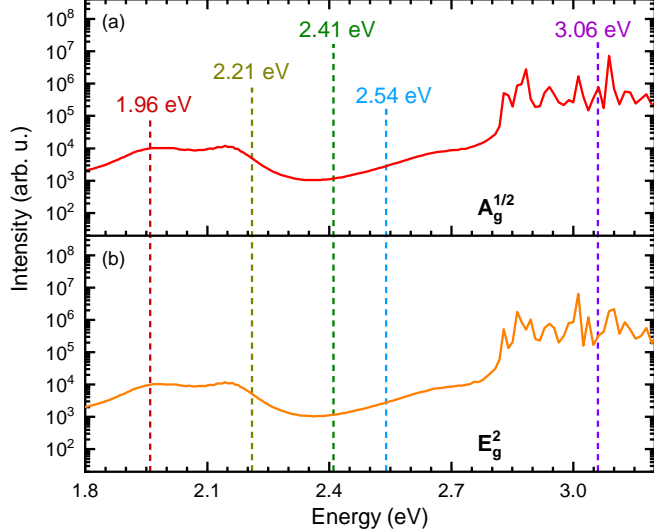


FIG. S5. Simulated enhancements of the $A_g^{1/2}$ and E_g^2 intensities using the transfer-matrix method. The colored vertical dashed lines indicate the excitation energies used in the experiment.

As shown in Fig. S5, the intensity dependence on excitation energy is very similar for both modes. Nevertheless, subtle differences are discernible, particularly in the high-energy range (2.8–3.2 eV), where the positions of the interference extrema do not align perfectly.

Despite these minor deviations, the overall enhancement of the $A_g^{1/2}$ and E_g^2 intensities is similar to that of the $A_g^{3/4}$ mode presented in Fig. 2 of the main text. As shown in Fig. S5(c), the simulated $A_g^{1/2}$ and E_g^2 intensities exhibit strong enhancement for excitation energies above approximately 2.85 eV, while reaching a minimum near 2.35 eV. These simulations therefore confirm that 3.06 eV is the optimal excitation energy for maximizing the Raman scattering response in the investigated CrCl_3 crystal, providing strong support for the discussion of interference conditions observed for the $A_g^{3/4}$ mode in the main text and enabling a more comprehensive description of the excitation-energy dependence of the Raman-mode intensities.

S4. Angle-resolved and excitation-dependent Raman spectra of an exfoliated CrCl_3 flake

Figure S6(a) shows polarization-resolved Raman spectra of a thick exfoliated CrCl_3 flake with a thickness of approximately 227 nm, acquired in co-linear and cross-linear configurations (sample details are provided in the Methods section). The spectra confirm that the thick exfoliated CrCl_3 flake exhibits the same phonon mode symmetries as the bulk crystal (see Section S2). In particular, the low-frequency E_g^1 mode is not resolved in these measurements.

To determine the symmetry of the Raman-active modes in the exfoliated CrCl_3 flake, we measured their linear polarization dependence at low temperature ($T=5$ K). The intensities of the Raman modes shown in Figs. S4(c), (d), and (e) are independent of the polarization angle. These modes are therefore assigned to the E_g symmetry and correspond to in-plane atomic vibrations within the crystal lattice. In contrast, the modes displayed in Figs. S4(b) and (e) exhibit a pronounced polarization dependence and their angular evolution was fitted using Eq. (5). These modes are accordingly assigned to the A_g symmetry and are associated with out-of-plane atomic vibrations.

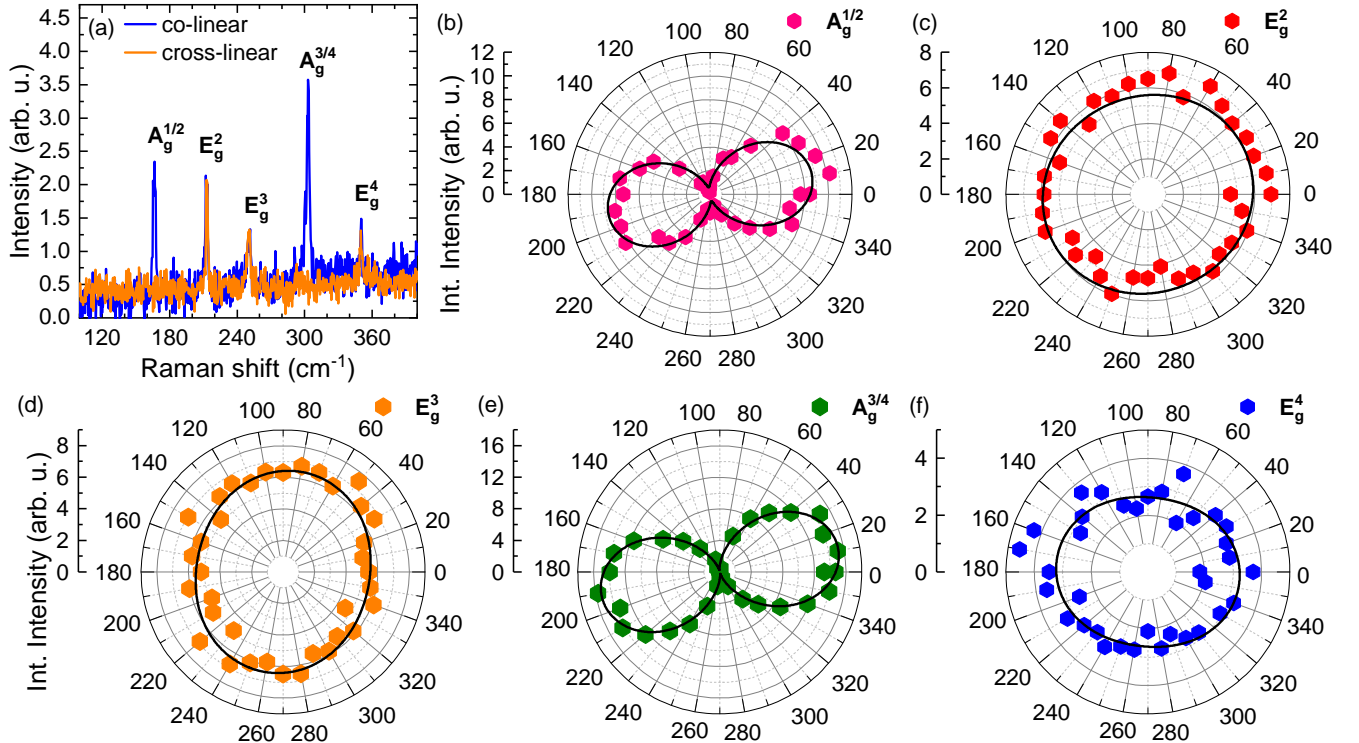


FIG. S6. (a) Low-temperature ($T=5$ K) Raman spectra of CrCl_3 flake measured in co-linear and cross-linear polarization configurations, using 3.06 eV laser excitation, with the power of 75 μW . The modes in panels (b) and (e) are a A_g type, while the modes in panels (c), (d) and (f) are the E_g type. The black curve represents the fitted formula using Eq. 5.

Figure S7(a) presents Raman spectra of an exfoliated CrCl_3 flake acquired using excitation energies of 1.96, 2.21, 2.41, 2.54, and 3.06 eV. Although the experimental conditions were identical to those used for the CrCl_3 crystal, pronounced differences in the relative intensities of the Raman modes are observed. In contrast to the crystal results shown in Fig. 2 of the main text, the intensity variation between the 3.06 eV excitation and the other excitation energies is much less pronounced. A strong reduction of the overall Raman intensity is observed only under 1.96 eV excitation. Moreover, the relative intensities among the Raman peaks change substantially, particularly for the $A_g^{1/2}$, E_g^2 , and E_g^3 modes.

To analyze the excitation-dependent intensity of the Raman modes, we deconvoluted the Raman spectra using Lorentzian functions. The integrated intensity of the $A_g^{1/2}$, E_g^2 , and $A_g^{3/4}$ peaks as a function of excitation energy is shown in Fig. S7(b). In contrast to the results obtained for the CrCl_3 crystal, presented in Fig. 2(b) of the main article, the highest intensity of phonon modes: $A_g^{1/2}$ and $A_g^{3/4}$ is apparent under the 2.54 eV and 3.06 eV excitations, While for the E_g^2 mode under 2.41 eV and also 3.06 eV. The intensities variation of the modes between the 2.54 eV and 3.06 eV excitations and the 2.41 eV and 2.21 eV ones is only about 2 times, while the intensity under 1.96 eV is substantially vanished.

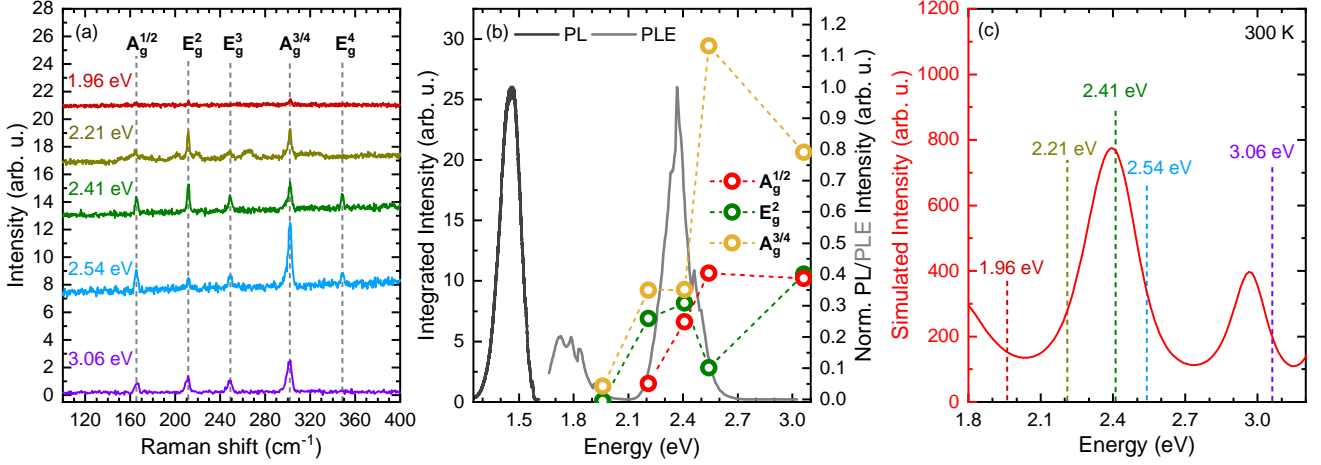


FIG. S7. (a) Raman scattering spectra of CrCl₃ thick flake exfoliated on the 285 nm SiO₂/Si substrate, measured at 5 K with different excitation energies: 1.96 eV, 2.21 eV, 2.41 eV, 2.54 eV, 3.06 eV, with an excitation power 50 μ W. The spectra have been vertically shifted for better visual clarity. (b) Left axis: graph shows points representing the intensity of the individual Raman modes A_g^{1/2}, E_g² and A_g^{3/4} collected with different lasers (in linear scale). Right axis: normalized PL (black), PLE (grey) spectra measured on the CrCl₃ flake. (c) Simulated enhancement of the A_g^{3/4} intensity using the transfer-matrix method. The colored vertical dashed lines indicate the excitation energies used in the experiment.

To examine the resonant conditions of Raman scattering, we measured the PLE spectrum of the CrCl₃ emission, as shown in Fig. S7(b). The PLE spectrum consists of two prominent features centered at approximately 1.8 eV and 2.4 eV. However, these resonances do not correlate with the excitation-energy dependence of the integrated phonon intensities. Consequently, the observed Raman enhancement cannot be understood in terms of conventional electron–phonon coupling leading to resonant Raman scattering.

As the PLE measurements, similarly to those for the bulk crystal discussed in the main text, do not sufficiently account for the enhancement profiles of the phonon modes in the exfoliated CrCl₃ flake, we simulated the excitation-energy dependence of the A_g^{3/4} intensity. The simulations were performed using the transfer-matrix method (TMM), following the same procedure as for the CrCl₃ crystal in the main text, and are shown in Fig. S7(c). The simulated spectrum consists of two enhancement features centered at approximately 2.40 eV and 2.95 eV, with an overall enhancement factor of about four between the maxima and minima. According to the simulation, the 2.41 eV excitation should yield the strongest Raman signal, whereas experimentally the highest intensities are observed under 2.54 eV and 3.06 eV excitation. Nevertheless, the lowest Raman intensity is predicted for 1.96 eV excitation, in agreement with the experimental results.

Because the simulations were carried out at 300 K, while the Raman measurements were performed at 5 K, the discrepancy between experiment and theory can be attributed to temperature effects. In particular, as discussed in Sec. S6, the integrated phonon intensities increase by approximately a factor of two when the temperature is raised from 5 to 300 K, which is comparable to the difference between the minimum and maximum values near the simulated enhancement peak at \sim 2.95 eV. Therefore, the deviation between the experimentally observed excitation-energy dependence of the phonon intensities and the simulated enhancement spectrum can be explained by the temperature-induced modifications of the electronic structure and phonon energies in exfoliated CrCl₃.

S5. Temperature evolutions of the Raman mode linewidths and intensities in CrCl_3 crystals.

Figure S8 presents the temperature dependence of the Raman modes observed in a CrCl_3 crystal over the temperature range of 5–300 K. Panels (a)–(f) show the temperature evolution of the full width at half-maximum (FWHM) of the phonon modes, while panels (g)–(l) display the corresponding evolution of their integrated intensities. In the following, we discuss in detail the temperature-dependent behaviors of both the FWHMs and the integrated intensities for all observed phonon modes.

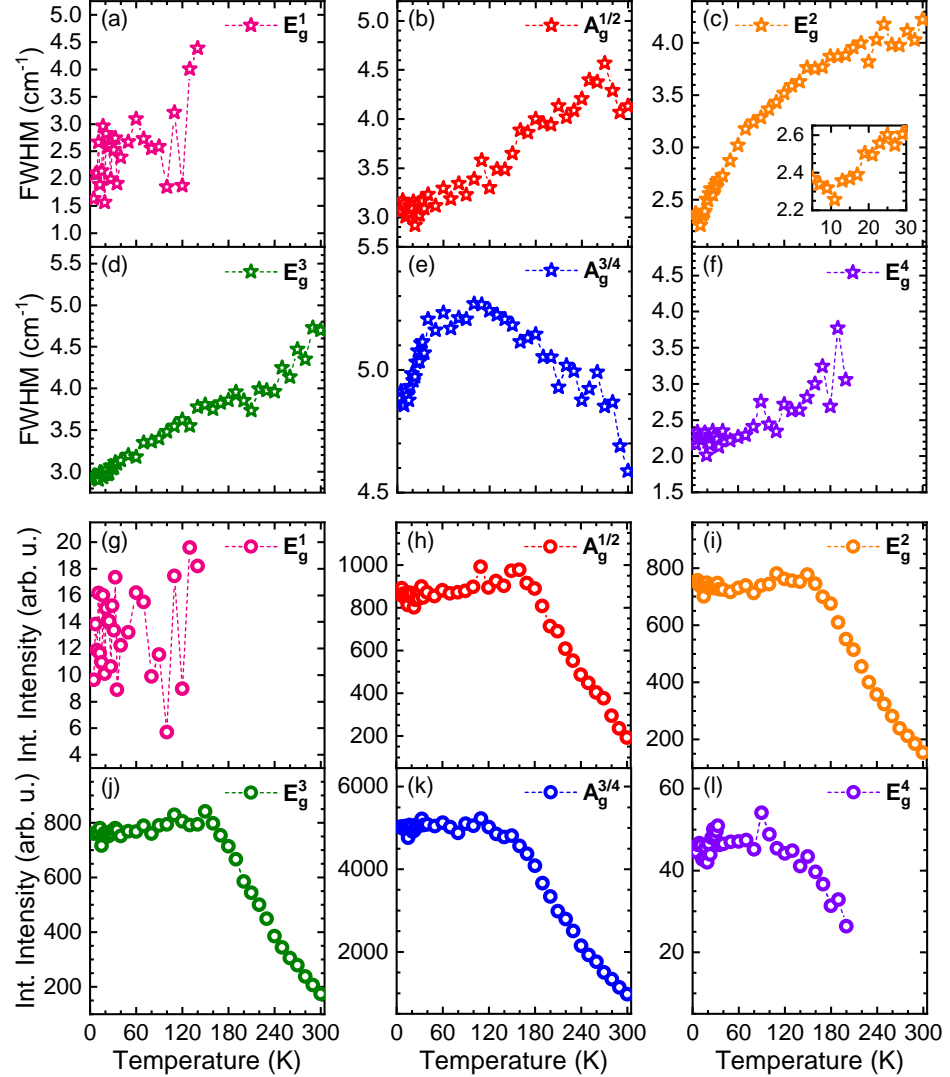


FIG. S8. Temperature dependencies of (a)–(f) the linewidths (full width at half maximum, FWHM) and (g)–(l) the integrated intensities of all phonon modes observed in the Raman spectra shown in Fig. 3 of the main text.

With increasing temperature, the FWHMs of all E_g modes, *i.e.*, E_g^1 , E_g^2 , E_g^3 , and E_g^4 , exhibit a clear monotonic increase, see Figs. S8(a), (c), (d), and (f). Such behavior is typical and can be attributed to lattice anharmonicity, arising from the combined effects of thermal expansion of the crystal lattice and enhanced phonon–phonon scattering processes.^{52,55–57,85} Subtle differences in the temperature evolution among the individual modes are also observed.

The behavior of the E_g^2 mode, shown in Fig. S8(c), is distinct from that of the other modes. Although the overall trend indicates thermal broadening, the low-temperature regime (5–30 K), highlighted in the inset, reveals an anomalous behavior. Specifically, the FWHM initially decreases upon warming, reaching a minimum at approximately 10 K, before increasing with further temperature growth. Notably, this minimum coincides with the proposed magnetic phase transition from the antiferromagnetic to a domain-like ferromagnetic order at the Néel temperature ($T_N \approx 14$ K).

The temperature dependencies of both A_g modes, *i.e.*, $A_g^{1/2}$ and $A_g^{3/4}$, shown in Figs. S8(b) and (e), are the most challenging to interpret. This difficulty arises because each Raman feature consists of two closely spaced modes that cannot be resolved under 3.06 eV excitation. Nevertheless, while the $A_g^{1/2}$ mode exhibits a temperature evolution similar to that of the E_g phonons, the behavior of $A_g^{3/4}$ is particularly intriguing. Its linewidth initially increases with temperature, reaching a maximum near 80 K, and subsequently exhibits an anomalous decrease. This behavior cannot be unambiguously assigned, as it may originate either from a structural phase transition from the $\bar{R}3$ to the $C2/m$ phase,^{13,51} or from the dual-peak nature of the mode itself: with increasing temperature, one component progressively weakens, leaving a single observable mode at room temperature.

The thermal evolutions of the integrated intensities of the observed phonon modes exhibit much smaller variations among the modes, as shown in Figs. S8(g)–(l). With the exception of the E_g^1 mode [Fig. S8(g)], which displays noticeable scatter likely due to its weak Raman intensity, the remaining modes, *i.e.*, E_g^2 , E_g^3 , E_g^4 , $A_g^{1/2}$, and $A_g^{3/4}$, exhibit very similar temperature dependencies. Their integrated intensities are only weakly affected by increasing temperature up to approximately 160 K, with modest enhancements observed for the $A_g^{1/2}$, E_g^2 , and E_g^3 modes. At higher temperatures, the integrated intensities decrease markedly, resulting in values approximately 5–8 times smaller at room temperature compared to those in the 5–160 K range. We attribute this pronounced reduction in intensity to the structural phase transition from the $\bar{R}3$ to the $C2/m$ phase,^{13,51} which may also induce concomitant changes in the electronic band structure of the CrCl_3 crystal.

S6. Temperature-dependent Raman spectra of an exfoliated CrCl_3 flake.

Figure S9 presents temperature-dependent Raman measurements performed on an exfoliated CrCl_3 flake. Panel (a) shows a false-color intensity map illustrating the evolution of the Raman spectrum over the temperature range from 5 K to 300 K, together with a representative spectrum acquired at 5 K. Within the investigated spectral window, four prominent phonon modes are clearly resolved: $\text{A}_g^{1/2}$ ($\sim 166 \text{ cm}^{-1}$), E_g^2 ($\sim 210 \text{ cm}^{-1}$), E_g^3 ($\sim 248 \text{ cm}^{-1}$), and $\text{A}_g^{3/4}$ ($\sim 301 \text{ cm}^{-1}$).

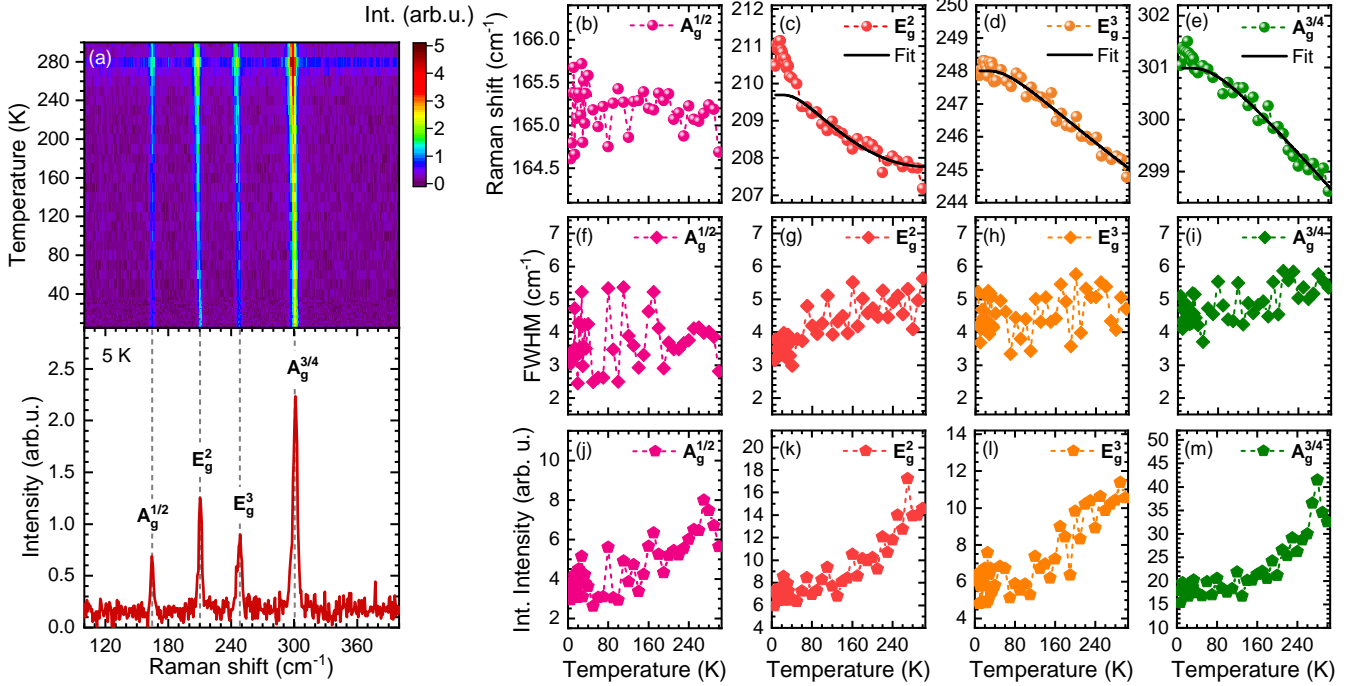


FIG. S9. (a) The top panel shows a false-color map of the Raman spectra of a CrCl_3 crystal, while the bottom panel presents the Raman spectrum measured at $T = 5$ K. Temperature dependence of (b)–(e) the Raman shifts, (f)–(i) the FWHMs, and (j)–(m) the integrated intensities of all observed phonon modes. The solid black curves in panels (b)–(e) represent fits using Eq. 1 described in the main text.

Panels (b)–(e) of Fig. S9 display the temperature dependences of the Raman shifts of the four observed phonon modes, extracted using Lorentzian fits to the Raman spectra. In general, the observed trends are similar to those shown in Fig. 3 of the main text for the CrCl_3 crystal. The experimental data were fitted using the Balkanski formula, given in Eq. 1 of the main text. All modes exhibit a monotonic redshift with increasing temperature, which is primarily attributed to the lattice anharmonicity arising from the combined effects of thermal expansion of the crystal lattice and enhanced phonon–phonon scattering processes.^{52,85}

The $\text{A}_g^{1/2}$ mode is significantly weaker than that measured in the bulk crystal, resulting in noticeable fluctuations of its Raman shift as a function of temperature (see Fig. S9(b)). Nevertheless, the characteristic redshift of the $\text{A}_g^{1/2}$ mode with increasing temperature is still observed. The temperature dependences of the E_g^2 and $\text{A}_g^{3/4}$ modes, shown in Figs. S9(c) and (e), respectively, are particularly notable and closely mirror the behavior observed in the bulk crystal. In the low-temperature regime (5–30 K), both the E_g^2 and $\text{A}_g^{3/4}$ modes exhibit an increase in Raman shift, reaching a maximum at 10 K, followed by a redshift at higher temperatures. As discussed in the main text, the anomaly at 10 K can be attributed to the proximity to the Néel temperature ($T_N = 14$ K) and is associated with the transition from the antiferromagnetic phase to a domain-like ferromagnetic phase. In contrast, the temperature evolution of the E_g^3 mode shows no detectable influence of spin–phonon coupling, as its behavior over the entire temperature range can be well described by the Balkanski model.

The temperature dependencies of the FWHMs for all four Raman peaks, shown in Figs. S9(f)–(i), exhibit substantial scatter. This effect is particularly pronounced for the $\text{A}_g^{1/2}$ mode, whose FWHM varies by more than a factor of two between consecutive temperature points separated by 20 K. For the remaining phonon modes, *i.e.*, E_g^2 , E_g^3 , and $\text{A}_g^{3/4}$,

an overall monotonic increase in FWHM with temperature can still be discerned, consistent with standard anharmonic lattice effects and enhanced electron–phonon interactions. However, this behavior lacks the specific features observed in the analogous analysis of the CrCl₃ crystal, as discussed in Sec. S5.

The influence of temperature on the integrated intensities of the phonon modes, shown in Figs. S9(j)–(m), is similar for all modes, *i.e.*, their intensities increase by approximately a factor of two upon warming from 5 to 300 K. This behavior is markedly different from that observed for the CrCl₃ crystal, presented in Figs. S8(g)–(l). As shown in Fig. S7(c), the 3.06 eV excitation lies on the slope of the enhancement peak centered at approximately 2.95 eV. Simulations indicate that the minimum and maximum intensities in the vicinity of this peak can differ by about a factor of two, which may account for the observed variation in phonon intensities. Consequently, given that temperature modulates both the electronic structure and the phonon energies, and considering possible quantitative discrepancies between experimental results and theoretical calculations, we primarily attribute the observed temperature evolution to the interference effect discussed in Sec. S4.